Earth and Planetary Science Letters 603 (2023) 117975

Contents lists available at ScienceDirect

Earth and Planetary Science Letters

journal homepage: www.elsevier.com/locate/epsl

Plate tectonics in action in the Mesoarchean: Implication from the Olondo greenstone belt on the Aldan Shield of Siberian Craton

Thi-Duyen Tran [a,b,c], Kuo-Lung Wang [b,d,*], Victor Kovach [e], Alexander Kotov [e], Sergey Velikoslavinsky [e], Nikolay Popov [f], Sergey Dril [g], Zhu-Yin Chu [h], Der-Chuen Lee [b], Li-Wei Kuo [c], Yoshiyuki Iizuka [b], Hao-Yang Lee [b]

[a] Taiwan International Graduate Program (TIGP) - Earth System Science Program, Academia Sinica and National Central University, Taipei, Taiwan
[b] Institute of Earth Sciences, Academia Sinica, Taipei, Taiwan
[c] Department of Earth Sciences, National Central University, Taoyuan, Taiwan
[d] Department of Geosciences, National Taiwan University, Taipei, Taiwan
[e] Institute of Precambrian Geology and Geochronology, Russian Academy of Sciences, St. Petersburg, Russia
[f] Institute of Petroleum Geology and Geophysics, Siberian Branch, Russian Academy of Sciences, Novosibirsk, Russia
[g] Institute of Geochemistry, Siberian Branch, Russian Academy of Sciences, Irkutsk, Russia
[h] State Key Laboratory of Lithospheric Evolution, Institute of Geology and Geophysics, Chinese Academy of Sciences, Beijing, China

ARTICLE INFO

Article history:
Received 10 March 2022
Received in revised form 19 December 2022
Accepted 22 December 2022
Available online 9 January 2023
Editor: R. Hickey-Vargas

Keywords:
Aldan Shield
Olondo greenstone belt
ultramafic-mafic rocks
arc signature
Mesoarchean
plume-induced subduction initiation

ABSTRACT

The Archean Olondo greenstone belt (OGB) is located on the Aldan shield, the largest basement of the Siberia craton. With well-preserved abundant mafic-ultramafic rocks, $\geq$ 30% in volume, the OGB is unique among other greenstone belts in the world. In this study, we present the most up-to-date geochemical and isotopic data for the ultramafic-mafic rocks of the OGB, in order to better constrain their mantle sources and the plate tectonic process involved in the formation of OGB at ca. 3 Ga. The ultramafic rocks vary from fresh to serpentinized dunites, and are highly refractory as residual mantle phase as indicated by depletion in P-Platinum Group Elements (PGE) relative to I-PGEs for highly siderophile elements (HSE). Fresh dunites show U-shaped rare earth element (REE) patterns, with positive to negative Nb anomalies, indicative of late metasomatism in their mantle source. Rhenium-Osmium isotopic compositions of these dunites yield mantle model age (T_{MA}) of 2960–3020 Ma, comparable to the formation age of the OGB at ca. 3 Ga. Together, the data suggest that, unlike mantle cumulate origin for most of the Archean ultramafic rocks, the OGB dunites were mantle residuals after a high degree of partial melting (>30%), which subsequently interacted with the subduction-related melt/fluid. On the other hand, the OGB mafic rocks including komatiitic and tholeiitic basalts show geochemical characteristics relative to the ultramafic residuals that reinforce a subduction-related regime as their formation setting, despite extra mid-ocean ridge and plume settings. Tholeiitic basalts yield variable REE patterns from depleted, chondritic, to enriched light rare earth elements (LREE) patterns, with variable Nb-Ta anomalies, indicating their similarities with modern N-MORB and boninites, comparable to mafic rocks in typical supra-subduction zone (SSZ) ophiolites. Such mafic rocks with combined lower $\varepsilon_{Nd}(t)$ and negative Nb-Ta anomalies were most likely the result of mixing with subducted components, consistent with the observed Nb depletion in the residual dunites. The Al-depleted komatiitic basalts may have originated from deep mantle source, corresponding to garnet stability field, confirmed by their depletion in HREE and requiring a mantle plume to transport and melt at such a depth. The OGB ultramafic-mafic rocks could be a record to witness plume-induced subduction initiation processes such that mantle plume, sea-floor spreading and subduction were all in operation in the Mesoarchean time.

1. Introduction

A greenstone belt is defined as an Archean to Proterozoic terrane, which is composed of associated metamorphic, plutonic, volcanic, and sedimentary rocks surrounded by granitoid plutons (de Wit, 2004; Furnes et al., 2014). Archean greenstone belts pre-

* Corresponding author at: Institute of Earth Sciences, Academia Sinica, 128 Sec. 2 Academia Road, Nankang, Taipei 11529, Taiwan.
E-mail address: kwang@earth.sinica.edu.tw (K.-L. Wang).

https://doi.org/10.1016/j.epsl.2022.117975
0012-821X/

serve important information about the Earth's history; therefore, understanding the formation of greenstone belts is essential for understanding the early evolution of the Earth. Over the past two decades, numerous studies with high-quality geochemical data have been conducted to explain the mantle source and geodynamic setting of greenstone belts. However, there are different ideas about the onset of plate tectonics on Earth. The subduction process might have started early from the Eoarchean (e.g., Nutman and Friend, 2009; Komiya et al., 2015; Garde et al., 2020; Hyung and Jacobsen, 2020; Nutman et al., 2020, 2021a, 2021b; Kusky et al., 2021; Windley et al., 2021; Grocolas et al., 2022), or Paleo- to Mesoarchean (Hanmer and Greene, 2002; Næraa et al., 2012; Grosch and Slama, 2017), even much later in Neoproterozoic time (Stern, 2005). Located in the Aldan Shield of the Siberia Craton, the Olondo Greenstone Belt (OGB) formed around 3.0 Ga (Nutman et al., 1992; Puchtel et al., 1993; Jahn et al., 1998; Kovach et al., 2020), which may provide key constraints on the evolution history of plate tectonics on Earth. In addition, the OGB has abundant mafic-ultramafic rocks (>30%; Puchtel and Zhuravlev, 1993; Popov et al., 1995) compared to other greenstone belts worldwide, offering us a unique opportunity to understand the mantle dynamics of the Earth during the Mesoarchean.

Due to poor accessibility, the most recent studies on geochemistry of the OGB were nearly two decades old. Grachev and Fedorovsky (1981) first proposed that the OGB resulted from continental rifting, similar to that under the modern tectonic regime. Popov et al. (1995) suggested that the OGB rocks were formed in different settings as combined with microcontinent–island arc–oceanic basin–microcontinent-like modern tectonic regimes, based on structure-metamorphic and lithostratigraphic studies. Puchtel (2004) emphasized the boninite-like geochemical signatures of the OGB ultramafic-mafic rocks, thus attributed them to the modern suprasubduction zone (SSZ)-like ophiolites. These different views were the results of limited geochemical and geochronological data reported for the OGB rocks (Bibikova et al., 1984; Popov et al., 1995; Puchtel and Zhuravlev, 1993; Puchtel et al., 1993; Puchtel, 2004). More detailed dating results, field observations with petrochemical studies of the OGB rocks were recently summarized by Jahn et al. (1998) and Puchtel (2004). This study focuses on major and trace elements (including highly siderophile elements (HSE; containing Platinum Group Element (PGE) and Re)) and Sm-Nd and Re-Os isotopic compositions of the OGB mafic-ultramafic rocks, newly collected since 2016, to study the age, mantle source characteristics, and formation of these rocks. The results should provide critical constraints on where and how the OGB formed during the Mesoarchean, and whether the plate tectonic had started on Earth then.

2. Geological setting

The Aldan Shield is situated in the southern part of the Siberian Craton, which constitutes an elongated trapezoid ca. 1200 km long (E–W) by 300–400 km across (Fig. 1a). The Aldan province incorporates the Olekma (in the west) and the Batomga (in the east) granite–greenstone terranes, separated by the West Aldan and Uchur (East Aldan) granulite–gneiss terranes (Kotov, 2003; Rosen and Turkina, 2007). The Olekma granite–greenstone terrain (OGGT) is characterized by the occurrence of N–S trending greenstone belts, surrounded by gray gneisses of tonalite–trondhjemite–granodiorite (TTG) compositions. Contacts between the supracrustal rocks and the surrounding tonalitic-trondhjemitic gneisses are tectonic. The gray gneiss domains are separated by four longitudinal greenstone belts that extend for 300 km in length and up to 30 km in width. Part of the gneiss protoliths formed as early as the Paleoarchean, evidenced by SHRIMP U–Pb zircon dates of 3212 ± 8 Ma (Nutman et al., 1992), whereas ages of gneisses range from 2.97 to 3.06 Ga, with the majority dated at ca. 3.0 Ga (Neymark et al., 1993; Salnikova et al., 1996; Jahn et al., 1998; Kotov, 2003; Velikoslavinskii et al., 2018). Both the greenstone belts and TTG gneisses were intruded by younger Meso- and Neoarchean to Paleoproterozoic granitoids.

In the greenstone belts, mafic metavolcanics of both tholeiitic and calc-alkaline affinities, and carbonate-terrigenous rocks usually occur (Rundqvist and Mitrofanov, 1993). Our study focuses on the OGB, which is the southern fragment of the Tokko-Khani greenstone belt (Fig. 1a), distinguished by the presence of high volume of mafic-ultramafic metavolcanics and intrusive rocks (Popov et al., 1990, 1995; Puchtel and Zhuravlev, 1993; Puchtel et al., 1993; Jahn et al., 1998). The OGB has the V- or Y-shape body of about 40 km long and a maximum width of 10 km. It is bounded from the west and east by subvertical oblique-slip reverse faults of the sub-longitudinal and northeastern strike. Contacts between the OGB rocks and surrounding TTG gneisses are tectonic (Figs. 2a and 2b). Tonalite and trondhjemite bodies intruded along the contacts. The OGB composed of metamorphosed mafic-ultramafic and intermediate-felsic volcanogenic, sedimentary and plutonic rocks (Fig. 1b). The volcanogenic rocks are divided into two units: komatiite–basalt and andesite–dacite (Popov et al., 1995). Because the boundaries between the komatiite–basalt and andesite–dacite sequences are syn-metamorphic surfaces, which could be pre-metamorphic faults of different ages (Popov et al., 1990, 1995; Bogomolova, 1993), the relative sequence of their formation has yet been established. Popov et al. (1990) suggested that komatiite-basalt sequence is in allochthonous occurrence thrusting over the andesite-dacite sequence. The OGB rocks were deformed and metamorphosed under greenschist to upper amphibolite facies during five stages of deformations including formation of thrusts (Bogomolova, 1993; Smelov et al., 2012).

The komatiite–basalt unit occurs at the margin of the belt with a maximum thickness of ∼ 500 m that covers > 30% area of the OGB (Figs. 1b, 2c-e). It is dominated by amphibole–plagioclase and amphibole schists (tholeiitic basalts and tuffs as protoliths), chlorite–actinolite and actinolite–chlorite schists (komatiitic basalts and komatiites as protoliths), and carbonate–actinolite schists (komatiite and komatiite tuffs as protoliths). The whole-rock Sm–Nd isochron age of 2973 ± 48 Ma ($\varepsilon_{Nd}(t)$ = 2.2 ± 0.1) was determined for komatiitic and tholeiitic metabasalts, and metagabbro from the eastern part of the OGB (Puchtel and Zhuravlev, 1993).

The andesite–dacite unit is exposed in the central part of the belt with intercalations of volcaniclastic and metasedimentary rocks. Primary effusive structure and textures, such as relict of highly deformed pillow lavas-like textures, are preserved indicating their volcanic origin. This unit consists of mainly amphibole, biotite–amphibole, and biotite microgneisses, which is considered as metamorphosed andesites, dacites, tuffs, tuffaceous sandstones, and sandstones. The U–Pb age of bulk zircon fractions from metaandesite of this association is 2960 ± 70 Ma (Bibikova et al., 1984). Nutman et al. (1992) obtained U–Pb (SHRIMP) zircon ages of 2983 ± 6, 2998 ± 9 and 3006 ± 5 Ma for the OGB felsic metavolcanic rocks.

Numerous tectonic slabs of metaperidotites and metadunites are the most common units of the ultramafic plutonic rocks in the OGB, which have clear tectonic relationships with the country rocks as described by Puchtel (2004; Figs. 1b, 2f-h). The whole-rock Sm–Nd isochron age of peridotites from the Red Hill is 3003 ± 117 Ma ($\varepsilon_{Nd}(t)$ = 1.12 ± 0.1; Puchtel and Zhuravlev, 1993). The mafic plutonic rocks are made up of sill-like metagabbro bodies with a thickness of 50 to 350 m. Zircons from metagabbro have been dated by LA-ICP-MS at 3005 ± 10 Ma (Kovach et al., unpublished data). Differentiated gabbro–diorite–tonalite and diorite–tonalite intrusions cut through the earliest structural elements of metavolcanogenic and metasedimentary rocks of the

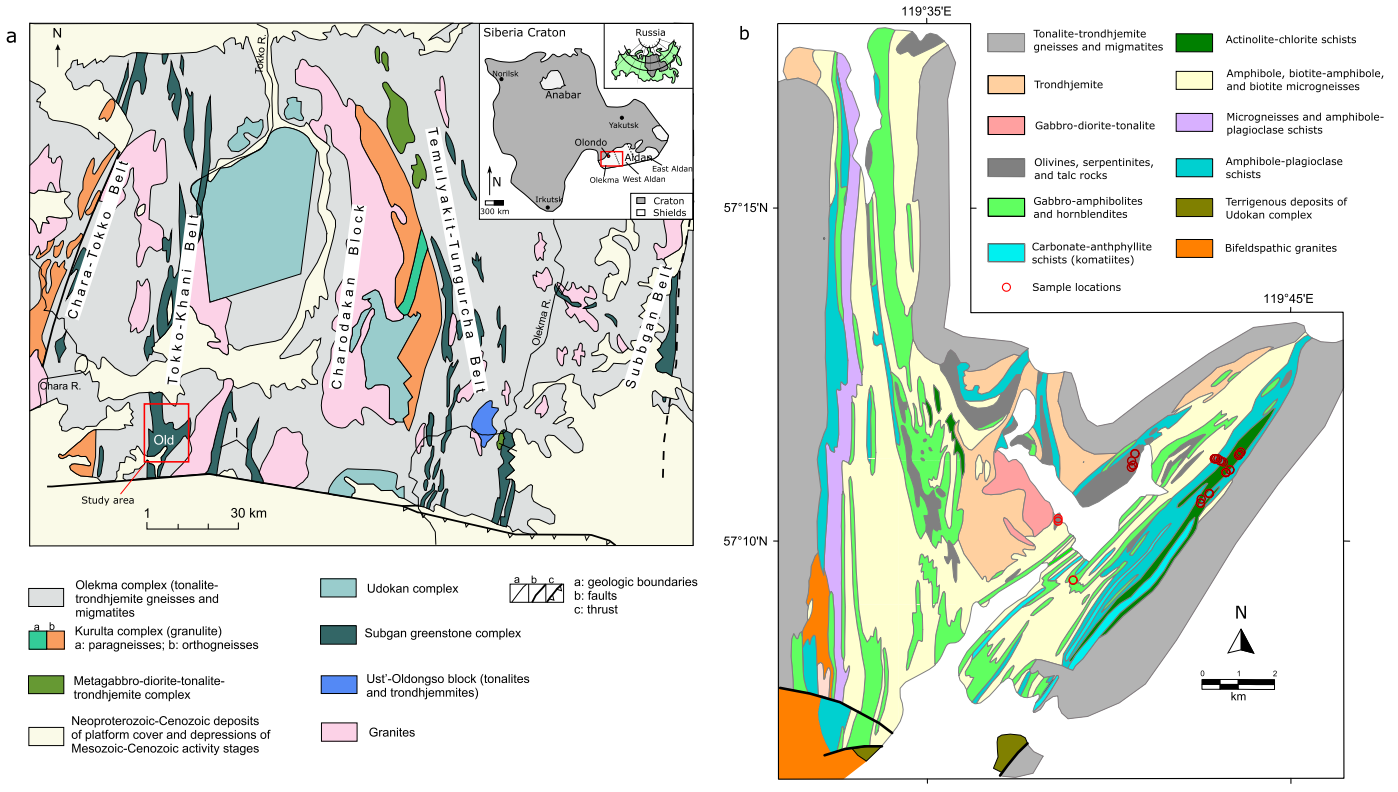

Fig. 1. (a) Geological map of the central and eastern parts of the western Aldan Shield indicating locations of the Olondo (within red square) and other greenstone belts. (b) Geological map of the Olondo greenstone belt (OGB) showing sample locations in red open circle in the eastern part where outcrops are best preserved and accessible. Both geological maps are modified after Smelov et al. (2012).

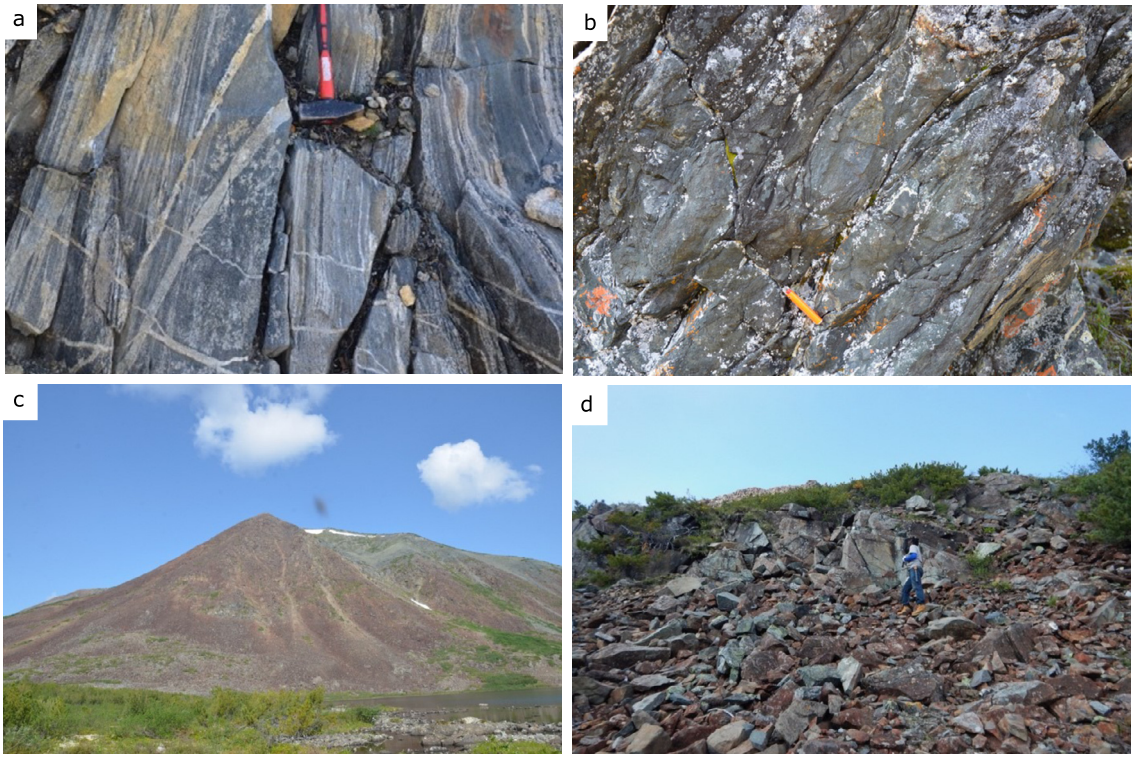

Fig. 2. The field photos including (a) strongly deformed foliations near the boundary between the OGB and Olekma TTG; (b) komatiitic basalt pillow lavas; (c) Red Hill made of ultramafic rocks with distinct reddish altered surface of dunites; (d) outcrop of OGB mafic rocks along the main road.

OGB (Fig. 1b) and contain xenoliths of metamorphosed and deformed mafic-ultramafic volcanic rocks. The U–Pb SHRIMP age of zircons from diorites is dated at 3018 ± 10 Ma (Nutman et al., 1992). Similar U–Pb ID-TIMS zircons ages of 3002 ± 5 and 3005 ± 7 Ma were obtained for metagabbro–diorite and quartz metadiorite intrusions (Kovach et al., 2020). These ages mark the

upper age boundary of the formation of the OGB supracrustal rocks.

3. Sample description and analytical methods

A total of 13 ultramafic and 39 mafic rock samples were collected from the Red Hill massif and along the eastern branch of the OGB, respectively. The ultramafic rocks are coarse-grained and altered to different levels, including dunite and serpentinite (Figs. S1a-d). Dunite is mainly composed of olivine with trace amount of spinel, showing a dark green to black color in the hand specimen. Primary spinels in dunites show euhedral crystals, whereas metamorphic spinels are anhedral and partially altered by serpentinization. Chemical zonation in spinels is attributed to pre-serpentinization metamorphism. The mafic metavolcanic rocks were all metamorphosed to greenschist and amphibolite (Figs. S1e-h). They display brown, dark, to pale green color in thin sections. Greenschists are composed of elongated fine-grained minerals such as amphibole, chlorite, epidote, quartz, and plagioclase. Detailed petrography descriptions are presented in Appendix A.

Whole-rock major- and trace-element have been analyzed for both ultramafic and mafic rocks. Selected ultramafic rocks were also determined for their whole-rock HSE concentrations and Re-Os isotopic compositions, as well as mineral compositions, whereas selected mafic rocks were measured for their whole-rock Sm-Nd isotopic compositions. Quantitative chemical analysis of olivine and spinel in the selected ultramafic rocks was conducted. All above-mentioned analyses were done at the Institute of Earth Sciences, Academia Sinica in Taipei, Taiwan and detailed method, instrumentation and analytical procedures are presented in Appendix A.

4. Results

4.1. Whole-rock major-element compositions

Whole-rock major and trace element data of the OGB rocks are listed in Table S1 and summarized in Table 1. The rocks were classified as dunite, serpentinite, komatiitic and tholeiitic basalts. Komatiitic basalts differ from komatiites by MgO content (<18 wt.% MgO for komatiitic basalts and 18-50 wt.% MgO for komatiites following Arndt et al. (2008)). Komatiites and peridotites other than dunites were not collected in this study but were reported by Puchtel et al. (1989) and Puchtel (2004). Their classifications are shown in the Zr/Ti vs. Nb/Y diagram (Fig. 3a; Winchester and Floyd, 1976) and Al–(Fe_{total} + Ti)–Mg diagram (Fig. 3b; Jensen and Pyke, 1982).

Dunites (1.2–8.7 wt.%) and serpentinites (15.5–22.8 wt.%) have higher LOI contents than komatiitic (1.0–1.7 wt.%) and tholeiitic basalts (0.4–4.5 wt.%), indicating of a more severe secondary alteration. Fresh dunites with LOI < 2 wt.%, have limited ranges of SiO_2 and MgO (43.4–50.4 wt.%), with Mg# from 82.0 to 90.1, low CaO, TiO_2, and Al_2O_3 contents (Table 1). Komatiitic basalts have a lower range of MgO (13.8–16.9 wt.%) with Mg# from 69.1 to 73.0. They are characterized by low concentration of Al_2O_3 and low Al_2O_3/TiO_2 ratio, but high Cr and Ni contents. Tholeiitic basalts are characterized by higher SiO_2, TiO_2, and Al_2O_3 contents, but lower MgO content (5.5–9.5 wt.%) and Mg# (from 41 to 61) than komatiitic basalts.

4.2. Whole-rock trace-element composition

The REE and trace-element diagrams of dunites and serpentinites are shown in Fig. 4. Most of their REE patterns display depletion in middle REE (MREE) with respect to LREE and HREE, showing concave-up or U-shaped patterns with slight depletion in LREE (Figs. 4a-b). Only dunite sample OL1633 exhibits an enriched LREE pattern. They all show negative Eu anomalies to different extent. Serpentinites (samples OL1644, OL1668, and OL1669) have higher REE abundances than most dunites, except for sample OL1633, whose LOI is high at 8.4 wt.%. In addition, slight enrichment of large-ion lithophile element (LILE) such as Th and LREE can be observed in the primitive mantle-normalized trace element patterns for all dunites and serpentinites. Some of them show negative Nb anomalies (Nb/La_n = 0.39–0.88, Nb/Yb_n = 0.38–0.91), with a lower positive Ti anomaly (Ti/Ti^* = 0.77–2.38) than those without negative Nb anomaly (Nb/La_n = 1.01–2.45, Nb/Yb_n = 0.78–1.50, Ti/Ti^* = 1.36–3.63 (Table 1 and Figs. 4c-d).

Komatiitic basalts are distinct from tholeiitic basalts by the depletion of HREEs (Gd/Yb_n = 1.01–1.53). They display slightly depleted to flat LREE in chondrite-normalized REE patterns (Fig. 5a). Normalizing to the primitive mantle (PM) (Fig. 5b), they show negative Nb and Ti anomalies and negative to positive Eu anomalies.

Tholeiitic basalts can be divided into three groups according to their distinct REE patterns: depleted tholeiites, chondritic tholeiites, and enriched tholeiites (Figs. 5c, e, g; Table 1). All three groups have flat HREE pattern with similar Gd/Yb_n ratio but different LREE enrichment. In the chondrite-normalized diagrams, depleted tholeiites show a similar LREE-depleted pattern to that of N-MORB, whereas chondritic tholeiites have a flat and enriched tholeiites display an LREE-enriched pattern. These tholeiites also show different spectrums from depleted (Th/Yb_n = 0.43–1.29; Nb/La_n = 0.61–1.00), to chondritic (Th/Yb_n = 1.17–1.40; Nb/La_n = 0.52–0.80), then enriched tholeiites (Th/Yb_n = 1.76–3.22; Nb/La_n = 0.37–0.61) in La and Th enrichment and Nb-Ta depletion in the PM-normalized spidergrams (Figs. 5d, f, h). Slightly negative to positive Eu anomalies are also observed in different tholeiites (Figs. 5c, e, g; Table 1), whereas slightly positive Zr–Hf anomalies can be only observed in enriched tholeiites (Fig. 5h).

4.3. Whole-rock Sm-Nd isotopic compositions of mafic metavolcanic rocks

Whole-rock Sm–Nd isotopic compositions of the mafic metavolcanic rocks are presented in Table S2. In brief, the komatiitic basalts have $^{147}Sm/^{144}Nd$ from 0.1923 to 0.2066 and $^{143}Nd/^{144}Nd$ from 0.512620 to 0.512939, and initial $^{143}Nd/^{144}Nd$ vary from 0.508819 to 0.508897, while $\varepsilon_{Nd}(t)$ vary from +1.4 to +2.9 at 3.0 Ga. Tholeiitic basalts have $^{147}Sm/^{144}Nd$ ranging from 0.1704 to 0.2316 and $^{143}Nd/^{144}Nd$ from 0.512216 to 0.513446. Their initial $^{143}Nd/^{144}Nd$ vary from 0.508826 to 0.508944, and $\varepsilon_{Nd}(t)$ range from +1.4 to +3.8 (Fig. S2). There is, however, no systematic variation in Nd isotopic compositions among different rock types.

4.4. Whole-rock highly siderophile element (HSE) compositions and Re-Os isotopic ratios of ultramafic rocks

The HSE concentrations of dunites and serpentinites are presented in Table S3. Dunite sample OL1633 has the lowest Os and Ir (I-PGE) and the highest Pt, Pd, and Re (P-PGE; Ir/(Pt+Pd) = 0.05) contents among all. Serpentinites (OL1668 and OL1669) have higher Pt, Pd and Re contents than dunite (Ir/(Pt+Pd) = 0.17–0.52). In the chondrite-normalized HSE diagram, most samples exhibit fractionated patterns that are strongly depleted in P-PGE (Figs. 4e and 4f). Dunite sample OL1633 is depleted in I-PGE and enriched in P-PGE, which is distinct from all others (Fig. 4f). In general, the PGE contents (except for Ru) of the dunites and serpentinites are lower than those of the primitive mantle.

The Re-Os isotopic ratios of dunites and serpentinites are presented in Table S3. The initial Os isotopic ratios are calculated based on the formation ages of the OGB at 3.0 Ga. The detailed parameters and calculations for the initial Os isotopic

Table 1
Summary of whole-rock major and trace element data of the OGB mafic-ultramafic rocks.

	Komatiic basalt (n=6)	Depleted tholeiite (n=17)	Chondritic tholeiite (n=9)	Enriched tholeiite (n=7)	Ultramafic dunite (n=10)	Ultramafic serpentinite (n=3)
SiO_2 (wt.%)	47-50	47-53	48-51	49-53	38-40	30-36
TiO_2	0.7-0.8	0.6-1.4	0.7-1.1	0.6-0.6	0-0.1	0.1-0.2
Al_2O_3	6.5-7.6	13.7-17.6	13.8-15.2	14-15.3	0.1-3	0.2-3.2
Fe_2O_{3t}	13.4-14.5	10.3-15.4	12.2-14.7	10.5-12.7	9.7-17	11.1-16.4
MnO	0.2-0.2	0.2-0.3	0.2-0.3	0.2-0.2	0.1-0.2	0.1-0.2
MgO	13.8-16.9	5.5-9.5	6.4-8.8	6.2-7.7	36.7-50.4	31.7-33.8
CaO	9.6-12.6	8.6-13	8.6-12.8	9.1-12.1	0.1-1.8	0.2-3
Na_2O	0.44-0.67	1.31-3.8	1.02-2.79	0.79-2	–	–
K_2O	0.06-0.15	0.08-0.36	0.08-0.31	0.08-0.33	–	–
P_2O_5	0.05-0.08	0.05-0.12	0.06-0.11	0.07-0.08	0.02-0.03	0.02-0.03
LOI	0.98-1.66	0.35-1.58	0.48-4.54	0.53-1.15	1.2-8.71	15.48-22.78
Mg#	67-71	41-61	46-58	53-58	83-91	80-85
Total	98.6-99.7	99-100	98.9-103.6	98.6-99.8	99.3-101.5	101.2-102.6
Sc (ppm)	39.9-48	32.8-66.6	35.3-63.5	36.7-66.5	5.9-29.6	7.8-578.2
Ti	4060-4935	3913-8527	4558-6537	3444-3941	49-651	70-776
V	172-200	212-343	243-291	224-253	6-63	48-4535
Cr	1110-1566	72-839	70-435	124-276	1847-7527	100-2543
Co	69-82	39-68	46-65	45-68	126-174	105-1610
Ni	346-492	57-179	81-147	68-113	1241-3140	12-2249
Cu	8-151	3-160	33-275	24-176	1-8	10-95
Zn	89-151	50-170	71-180	90-166	34-84	3-58
Ga	8.84-11.12	11.40-18.79	14.50-17.46	13.60-15.7	0.38-3.57	0.03-3.77
Rb	0.43-3.49	0.70-2.72	0.64-8.25	0.69-17.9	0.03-0.17	0.04-5.45
Sr	22.8-56.4	89.1-243.4	88.3-155.2	101.9-182.3	0.2-3.2	0.9-14.9
Y	12.9-15.4	13.0-31.0	17.5-21.6	14.3-17.6	0.10-2.7	0.6-5.6
Zr	39.8-46.8	28.4-80	41.4-67.3	42.6-56.5	0.4-5.4	0.1-6.1
Nb	1.93-2.4	0.99-3.24	1.61-2.88	1.49-2.25	0.02-0.29	0.01-0.48
Cs	0.02-0.139	0.012-0.151	0.009-1.265	0.031-1.63	0.003-0.025	0.01-0.074
Ba	5.77-42.4	13.47-93.08	6.72-76.96	11.57-114	0.02-1.88	0.3-1.3
La	2.1-3.16	1.32-3.89	2.51-3.7	3.16-4.88	0.02-0.71	0.12-0.84
Ce	6.49-7.73	3.97-10.73	6.62-9.8	7.35-10.65	0.04-2.18	0.11-1.15
Pr	1.038-1.253	0.6-1.736	1.025-1.485	0.9-1.415	0.004-0.302	0.051-0.568
Nd	5.38-6.19	3.18-9.04	5.15-7.52	4.55-6.24	0.02-1.33	0.17-0.71
Sm	1.75-2.09	1.45-3.1	1.71-2.44	1.46-1.75	0.01-0.32	0.02-0.18
Eu	0.627-0.8	0.45-1.005	0.6-0.84	0.52-0.66	0.001-0.065	0.007-0.183
Gd	1.96-2.74	1.41-4.46	2.1-3.37	1.55-2.41	0.01-0.4	0.03-0.22
Tb	0.395-0.45	0.31-0.77	0.4-0.573	0.34-0.419	0.002-0.071	0.011-0.247
Dy	2.24-2.86	1.83-5.17	2.66-3.74	2.13-2.84	0.01-0.47	0.06-0.27
Ho	0.51-0.587	0.55-1.129	0.639-0.798	0.524-0.615	0.004-0.1	0.018-0.2
Er	1.4-1.63	1.31-3.3	1.67-2.28	1.36-1.84	0.01-0.3	0.04-0.19
Tm	0.201-0.244	0.21-0.491	0.21-0.344	0.23-0.291	0.003-0.044	0.016-0.215
Yb	1.32-1.49	1.53-3.18	1.87-2.18	1.53-1.89	0.03-0.3	0.03-0.25
Lu	0.19-0.22	0.2-0.47	0.28-0.33	0.23-0.33	0.01-0.05	0.03-0.14
Hf	1.16-1.35	0.83-2.31	1.23-1.86	1.09-1.5	0.01-0.17	0.01-0.16
Ta	0.12-0.17	0.05-0.23	0.13-0.2	0.11-0.19	0-0.02	0.01-0.08
Pb	0.31-17.9	0.25-123	2.07-32.2	1.85-7.52	0.03-1.37	0.05-0.16
Th	0.3-0.34	0.15-0.48	0.37-0.52	0.46-1.04	0.01-0.08	0.03-0.06
U	0.05-0.1	0.04-0.13	0.05-0.16	0.18-0.3	0-0.04	0.02-1.26
Th/Yb_n	1.23-1.39	0.43-1.29	1.17-1.4	1.75-3.22	1.21-3.69	1.43-3.23
Th/Nb_n	1.15-1.36	0.75-1.98	1.5-2.32	2.25-4.66	1.37-8.07	1.01-2.39
La/Yb_n	1.01-1.65	0.51-1.01	0.95-1.23	1.33-1.91	0.46-1.68	0.68-1.34
La/Sm_n	0.68-1.04	0.59-0.91	0.92-1.12	1.29-1.8	0.82-1.72	0.7-1.59
Gd/Yb_n	1.1-1.53	0.76-1.22	0.82-1.29	0.83-1.15	0.26-1.1	0.39-0.74
Nb/La_n	0.7-1.08	0.61-1	0.52-0.8	0.37-0.61	0.39-2.45	0.35-1.01
Nb/Yb_n	0.9-1.21	0.39-0.85	0.52-0.92	0.67-0.98	0.38-1.5	0.14-1.34
Eu/Eu^*	0.84-1.21	0.83-1.31	0.86-1.06	0.85-1.23	0.24-0.88	0.31-21.57
Ti/Ti^*	0.82-1.14	0.79-1.24	0.84-1.07	0.77-1.02	0.76-3.6	0.79-1.69
Ce/Ce^*	0.95-1.05	0.93-1.14	0.91-1.13	0.99-1.02	1.01-1.15	0.04-1.09

Mg# is calculated as the mole ratio of $Mg/(Mg + Fe^{2+})$, where Fe^{2+} is assumed to be 90% of the total Fe.
Selected elements are normalized to primitive mantle and chondrite (Sun and McDonough, 1989).
Eu anomalies (Eu/Eu^*) have been calculated as $Eu/Eu^* = (Eu)_{cn}/[(Sm)_{cn} \times (Gd)_{cn}]^{0.5}$.
Ce/Ce^*, and Ti/Ti^* anomalies are similarly calculated as $Ce/Ce^* = (Ce)_{cn}/[(La)_{cn} \times (Pr)_{cn}]^{0.5}$ and $Ti/Ti^* = (Ti)_{cn}/[(Gd)_{cn} \times (Dy)_{cn}]^{0.5}$.

ratios and model ages are described in the Appendix A. Except for OL1633, both dunites and serpentinites have subchondritic $^{187}Os/^{188}Os$ ratios, with dunites showing lower $^{187}Os/^{188}Os_i$ (0.10687–0.10744) than serpentinites ($^{187}Os/^{188}Os_i$ = 0.11600 and 0.11924). They also have subchondritic $^{187}Re/^{188}Os$, with dunites showing lower $^{187}Re/^{188}Os$ ratios (0.0048–0.2562) than serpentinites ($^{187}Re/^{188}Os$ = 0.2399–0.3020). The initial $^{187}Os/^{188}Os_i$ of the dunites range from 0.10638 to 0.10682, with γOs_i close to 0 (γOs_i = -0.17 to 0.13). These results are consistent with $^{187}Os/^{188}Os_i$ = 0.1058 ± 5 reported by Puchtel (2004). Serpentinites have lower initial $^{187}Os/^{188}Os_i$ (0.10371–0.10377) with γOs_i = -2.39 to -2.45, due to their higher $^{187}Re/^{188}Os$ relative to those of dunites. With a different HSE pattern, dunite sample OL1633 has the highest measured $^{187}Os/^{188}Os_m$ = 0.12251, median $^{187}Re/^{188}Os$ = 0.2562, and the highest initial $^{187}Os/^{188}Os_i$ = 0.10938 with γOs_i up to 2.89.

The calculated T_{MA} and T_{RD} (Re-depletion) model ages are similar for dunites from 2959 to 3020 Ma and 2914 to 2930 Ma

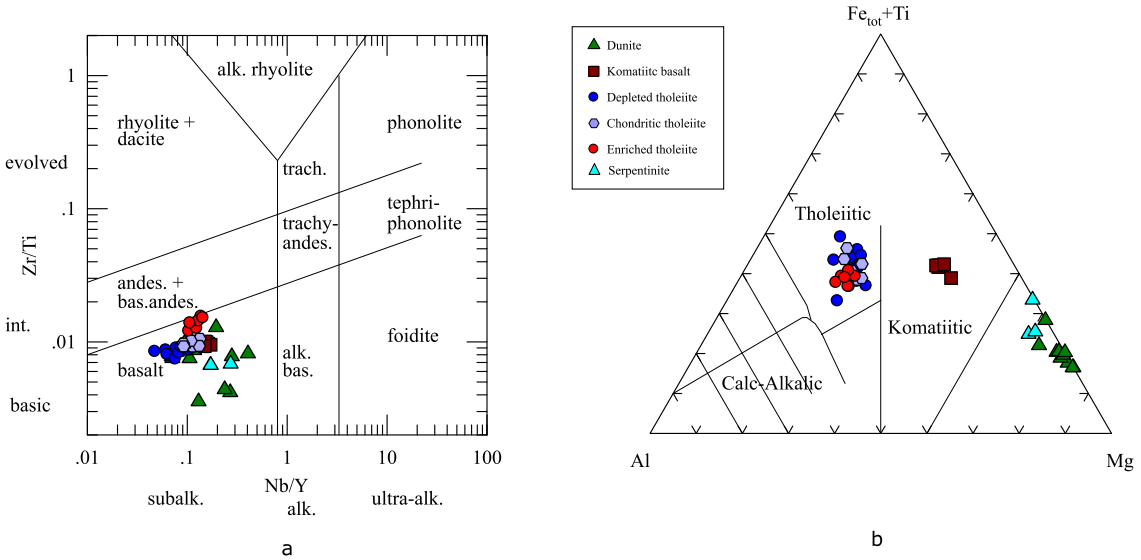

Fig. 3. Classification diagrams of the OGB rocks. (a) Zr/Ti vs Nb/Y diagram from Winchester and Floyd (1976) and (b) Al-(Fe_{total} + Ti)-Mg diagram from Jensen and Pyke (1982).

(Table S3), respectively, owing to their relatively low $^{187}Re/^{188}Os$ ratios. The average of these Os model ages is also close to the formation age of the OGB via the Sm-Nd isochron age at ca. 3.0 Ga (see above). Serpentinites yield older T_{MA} ages (3880 and 4309 Ma) but younger T_{RD} model ages (1250 and 1700 Ma). The difference between T_{MA} and T_{RD} model ages reflects their higher $^{187}Re/^{188}Os$ ratios. Dunite sample OL1633 has the youngest T_{MA} (2002 Ma) and T_{RD} (792 Ma) model ages, indicating the effects of secondary alteration and Re mobility that occurred long after the emplacement of the ultramafic body.

4.5. Mineral major-element compositions of ultramafic rocks

The EPMA data from 132-point analyses of olivines and 137-point analyses of Cr-spinels are listed in Supplementary Tables S4 and S5. In general, the olivines in fresh and slightly serpentinized dunites are characterized by high MgO (49-52 wt.% with Fo = 89.5 to 93.1; Fig. S3) with trace amounts of NiO, MnO, Cr_2O_3, and CaO. The most pristine dunite sample OL1639 shows a more homogeneous composition with Fo content range from 91.7–92.4. Spinels in dunites have a wide range of Mg# (36–5), Cr# (68–99), and TiO_2 content (0.08–1.96 wt.%; Tables S4 and S5). The spinels in the freshest dunite sample OL1639 have the lowest TiO_2 contents (0.08–0.28 wt.%). Aswad et al. (2011) recognized two types of Cr-spinels in serpentinites. Primary spinels have lower Cr# and higher Mg# than metamorphic spinels because Al^{3+} and Mg^{2+} are replaced by Fe^{3+} and Fe^{2+}, respectively, during serpentinization. In this study, spinels were also separated into two groups: primary spinels have Mg# of 36–29 and Cr# of 68–73, whereas metamorphic spinels have Mg# of 24–5 and Cr# of 75–99. Only the primary spinels were used as a petrogenetic indicator.

5. Discussion

5.1. Effects of secondary alteration, metamorphism, fractional crystallization and crustal contamination

Secondary alteration and metamorphism are widespread in Archean rocks, so their primary geochemical characteristics could be modified to various extent (Lahaye and Arndt, 1996; Polat et al., 2002; Polat and Hofmann, 2003). Thus, it is important to evaluate the effects of secondary alteration and metamorphism, particularly on relatively mobile elements. All OGB mafic rocks have less than 2 wt.% LOI, with the exception of chondritic tholeiite sample OL1617 (LOI = 4.5 wt.%), which indicates very limited secondary alteration on them. In contrast to mafic rocks, the six ultramafic dunites have higher LOI from 3.7 to 8.7 wt.% and the rest with < 2 wt.% LOI. Serpentinites originating from altered dunites show the highest LOI (15.5 to 22.9 wt.%). Serpentinites with higher REE abundances also have high LOI values, suggesting that secondary alteration might affect their trace element abundance. As a result, those dunites having lower LOI contents should reflect more primary features, as shown by their major-element compositions above. Although less primary minerals such as spinel were preserved in the serpentinites, their similar REE patterns as dunites suggest that the protolith of the serpentinite was dunite (Fig. 4).

During seawater alteration, Ce^{+4} may react with water that results in precipitation of CeO_2 and a negative Ce anomaly in the REE pattern (Braun et al., 1993). Polat et al. (2002) reported a range of Ce/Ce* ratios from 0.9 to 1.1 for Eoarchean to Mesoarchean ultramafic to mafic volcanic rocks in SW Greenland could suggest very limited LREE mobility. Except for serpentine sample OL1669, the OGB ultramafic-mafic rocks have Ce/Ce* ranging from 0.91 to 1.15 (Table 1), indicating that they were not significantly affected by seawater alteration. All the OGB dunites display negative Eu anomalies in their REE patterns (Fig. 4). This is uncommon for ultramafic rocks because under mantle condition, none of the major mineral, e.g., olivine, pyroxene, and spinel/garnet, is able to fractionate Eu. Not even plagioclase, existing in the mantle residual with high MgO (>10 wt.%) after melt extraction, is capable of fractionating Eu (Green and Ringwood, 1967; Sun and Nesbitt, 1978). A negative Eu anomaly could result from secondary alteration, as previously suggested by Jahn et al. (1998) for the OGB rocks. Our data show that the freshest dunite exhibits the lowest Eu anomaly (Eu/Eu* = 0.85), whereas the serpentinites with the highest LOI reveal the strongest negative Eu anomaly (Eu/Eu* = 0.35). Therefore, the negative Eu anomaly in the OGB ultramafic rocks is probably caused by secondary alteration. This is consistent with the lack of evidence for early formation of anorthosite in the OGB and/or nearby regions that might be responsible for the observed negative Eu anomaly.

Considering the high whole-rock Mg# of komatiitic basalts (67-71; Supplementary Table S1) which is close to that of primary magma (66∼75), fractional crystallization is neglectable. However,

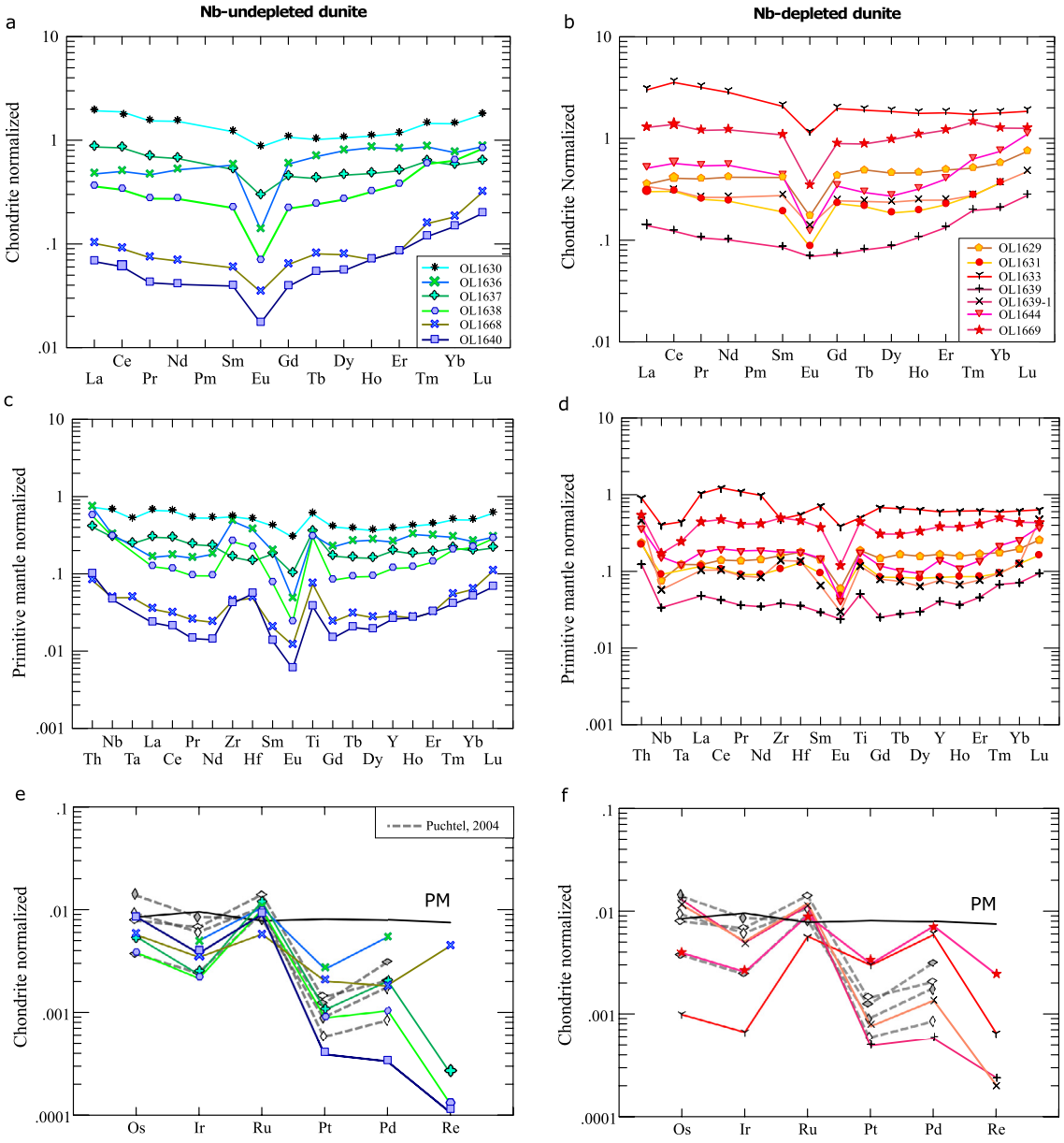

Fig. 4. REE patterns (a and b), multi trace-element diagrams (i.e., spidergrams; c and d) and HSE patterns (e and f) of dunites and serpentinites from the OGB. Normalizing chondrite and primitive mantle values are from Sun and McDonough (1989). Dunites showing Nb negative anomaly are plotted in the right panels (4a, 4c and 4e), whereas those not showing show Nb negative anomaly are in the left panels (4b, 4d and 4f). Gray dash lines indicate PGE data from Puchtel (2004) for comparison (4e and 4f).

fractional crystallization might still be present among the mafic rocks, although to a less extent. Whole-rock Mg# of the three types of tholeiites are 41 to 61 for depleted tholeiites, 46-58 for chondritic tholeiites, and 53 to 58 for enriched tholeiites. To avoid possible fractional crystallization effect, tholeiites with Mg# higher than 53 are chosen for petrogenesis discussion in the spidergrams (Fig. 5). Note that distinct REE and spidergram patterns of the three types of tholeiites could not result from fractional crystallization and degree of partial melting.

Negative Nb anomalies in the OGB mafic-ultramafic rocks, especially in enriched tholeiitic basalts, could reflect either crustal contamination or inherited mantle signatures. Although the OGB mafic rocks are characterized by positive initial Nd isotopic values ($\varepsilon_{Nd}(t)$~+2), they cannot be used as evidence against crustal contamination. The felsic rocks formed simultaneously with the OGB mafic-ultramafic rocks, which are regarded as local crustal components, yield similar positive Nd isotopic ratios (Jahn et al., 1998). However, the lack of correlation between increasing Mg# with decreasing ε_{Nd} and increasing La/Sm_n with decreasing Nb/Yb_n (Fig. 6), argues against any significant amount of crustal contamination for the OGB mafic rocks. In addition, the negative Nb anomaly is also observed in the residual dunites (will be discussed in the next section), which is most likely an inherited mantle source characteristic.

5.2. Petrogenesis and mantle source characters

5.2.1. Ultramafic rocks: Archean residue mantle and its age

Dunites can be formed as either an accumulation of olivine from a basaltic melt or residual phases after high degree of partial melting in the mantle; however, no obvious petrological evidence can be used to identify the OGB dunite with a cumulate origin. Olondo dunites have MgO contents with Mg# ranging from 82.0 to 90.1 and very low CaO, TiO_2, and Al_2O_3 but high Cr and Ni contents (Table 1). Olivines in fresh and slightly serpentinized dunites are characterized by high Fo contents (89.5 to 93.1; Fig. S3) with

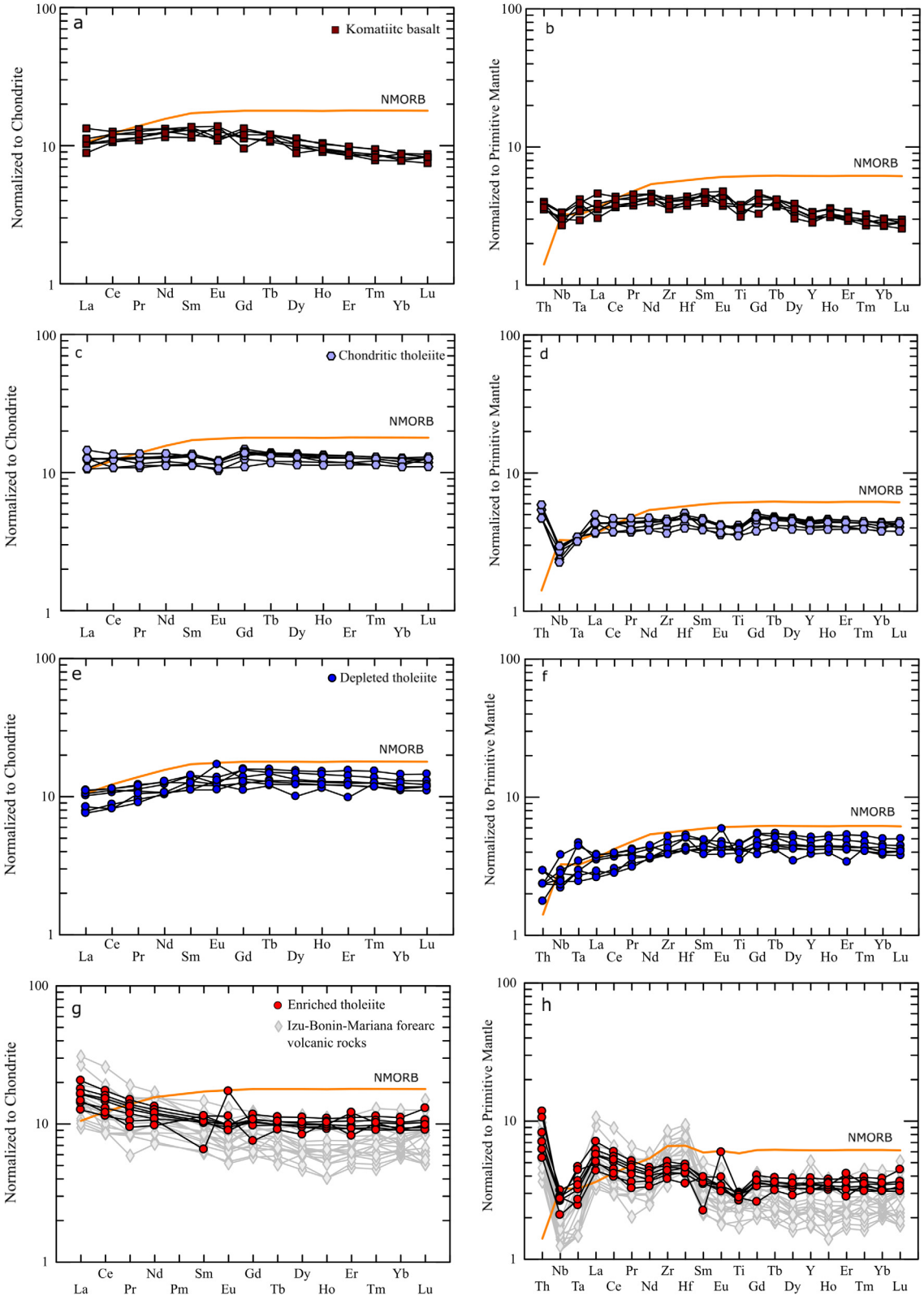

Fig. 5. Chondrite-normalized REE patterns (a, c, e and g) and PM-normalized spidergrams (b, d, f and h) for komatiitic and tholeiitic basalts from the OGB. Patterns of N-MORB and Izu-Bonin-Mariana fore-arc volcanic rocks from the drilling site 786 (Murton et al., 1992) are plotted for comparison. Normalized chondrite, N-MORB and PM values are from Sun and McDonough (1989).

the freshest dunite sample OL1639 showing high Fo content (91.7 to 92.4; Table S4). The primary euhedral spinels in dunites have a high Cr# of 68–73. In addition, except for sample OL1633 showing LREE-enriched patterns, all dunites and serpentinites have slightly U-shaped or concave-up REE patterns with depletion in MREE with respect to LREE and HREE, and La/Yb$<$1. The U-shaped or concave-up REE patterns of the dunites and serpentinites could not be formed from a single melting event. Instead, they can be better

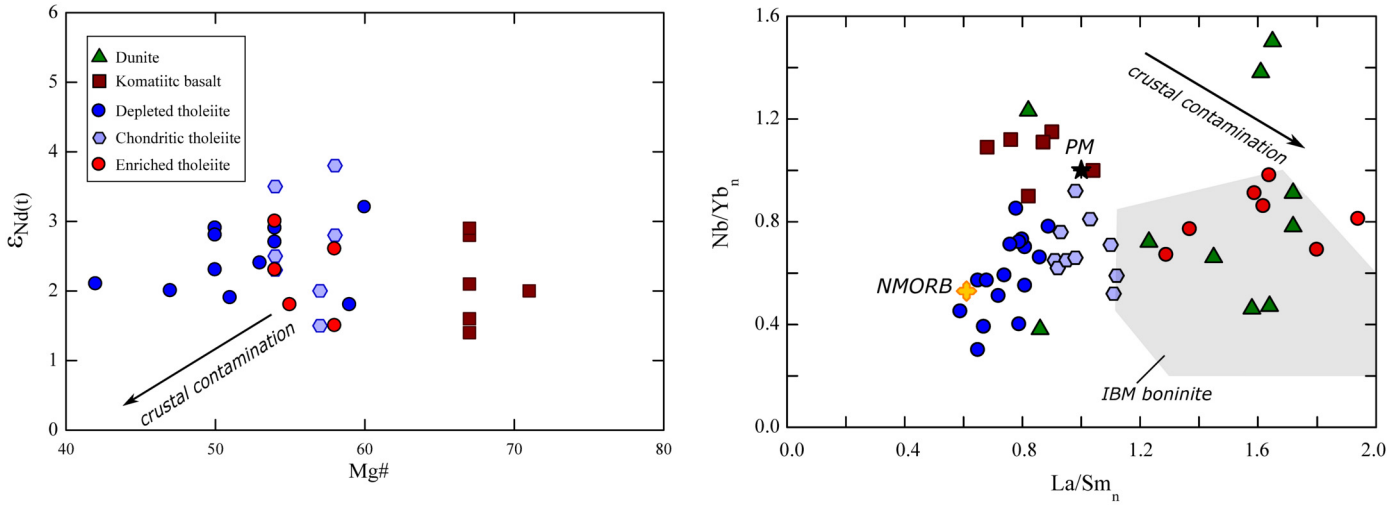

Fig. 6. Plots of $\varepsilon_{Nd}(t)$ vs. Mg# and Nb/Yb_n versus La/Sm_n ratios. No correlation between $\varepsilon_{Nd}(t)$ with Mg# contents and La/Sm_n with Nb/Yb_n ratio suggesting insignificant effect of crustal contamination.

explained by residual mantle rocks (depleted in LREE and MREE) metasomatized by later melts/fluid to re-enrich LREE. In addition, HSEs could be a powerful tool for distinguishing between the accumulated and residual phases. Because during partial melting, the compatible I-PGEs (Ir, Os, Ru) reside in the residual phases, whereas incompatible P-PGEs (Pt, Pd) tend to be removed by the melt. Also, unlike lithophile elements, HSEs are barely modified by secondary processes such as metasomatism, metamorphism, and alternation. Except for dunite sample OL1633 and serpentinite sample OL1669 (Pd/Ir = 3.7 and 10.8, respectively; Table S3), the HSE abundance of Olondo dunites and serpentinites exhibit enriched I-PGE patterns (Pd/Ir = 0.1–1.0; Table S3), consistent with a residual mantle origin. Furthermore, all dunites and serpentinites have subchondritic $^{187}Os/^{188}Os$ and $^{187}Re/^{188}Os$ ratios, which indicate their residual mantle affinity. Despite one dunite and all serpentinites displaying slightly higher $^{187}Re/^{188}Os$ that is most likely the result of late metasomatism. While most Archean ultramafic plutonic rocks in the world seem to have formed as mantle cumulates (e.g., Kusky et al., 2001; McIntyre et al., 2019; Szilas et al., 2018), the mantle residual origin for the Olondo dunites and serpentinites might further constrain the geochemical evolution of the upper mantle during the Mesoarchean.

The Nb depletion in the spidergram is observed in some OGB dunites (Fig. 4d), which is clearly not caused by crustal contamination but inherited characteristics from the residual lithospheric mantle. Trace-element characteristics of these OGB dunites indicate that later metasomatism by melt or fluid, to re-enrich LILE and LREE but not high field strength element (HFSE) such as Nb, had influenced the part of residual mantle after its forming by melt extraction. The potential metasomatic agent is most likely either the dehydration fluid or melt of subducted continental sediment, both related to subduction zone processes. It indicates that the residual lithospheric mantle where some OGB dunites were formed should be above the subducted slab to be metasomatized by either dehydration fluid or melt of subducted continental sediment as in the mantle wedge of modern subduction zone. This can be further supported by mineral chemistry of these dunites showing primary high-Fo olivines (90-93) and high-Cr# spinels (68–73), which are equivalent to the residual mantle after 30–40% degrees of partial melting and plot in the supra-subduction zone (SSZ) setting in the olivine-spinel mantle array (OSMA; Arai, 1994a; Fig. 7a). Furthermore, using olivine-spinel Fe-Mg exchange thermometry and oxygen barometry proposed by Ballhaus et al. (1991), the OGB dunites show average equilibrium temperature for primary spinels is $\sim 660 \pm 30\,^{\circ}C$ and slightly higher up to $>700\,^{\circ}C$ for metamorphic spinels (Fig. S4), and their $\Delta \log fO_2$ (FMQ) are between +1.2 and +2.3. Equilibrium temperatures of OGB dunites are similar to the average fore-arc peridotites in the modern Izu-Bonin-Mariana (IBM) subduction system calculated at $647 \pm 40\,^{\circ}C$ using the same olivine-spinel Fe-Mg exchange thermometry (Parkinson and Pearce, 1998). The estimated $\Delta \log fO_2$ (FMQ) for OGB is also close to that of the forearc dunites including the IBM and South Sandwich arc system (Pearce et al., 2000 and references therein). Thus, where some OGB dunites formed in the Mesoarchean time should be comparable to the mantle section in the modern mantle wedge above the subduction zone.

Some other OGB dunites do not display Nb depletion in the spidergram (Fig. 4c), although they also have slightly U-shaped or concave-up REE patterns (Fig. 4a), which could be the results of later metasomatism to re-enrich LILE and LREE only. Such metasomatic agent is different from the subduction components proposed above for the OGB dunites with Nb depletion in the spidergram. Considering the subtle enrichment of LILE and LREE, basaltic melt could potentially metasomatize this part of residual lithospheric mantle while it rose up to the surface from asthenospheric mantle.

Dating these residual dunites and serpentinites using the Sm–Nd isotopic system is challenging, due to their very low Sm–Nd concentrations, and are thus easily affected by subsequent magmatic events. The Re–Os isotopic system, however, could be more useful in this case because of its strong parent-daughter fractionation after partial melting, with high Os content in residual peridotite, and more resistant to late metasomatism and secondary alteration. The OGB dunites showing residual HSE patterns (Pd/Ir = 0.11–1.05; Figs. 4e and 4f) with low $^{187}Re/^{188}Os$ ratios (0.0048–0.0181) yield almost identical T_{MA} and T_{RD} model ages from 2959 to 3020 Ma and from 2914 to 2953 Ma, respectively (Table S3). Very low Re concentrations (close to zero) combined with similar T_{MA} and T_{RD} model ages suggest that the OGB residue dunites experienced negligible effect of subsequent melting events since its formation. Furthermore, these Os model ages are consistent with the formation age of the Olondo Greenstone Belt (ca. 3.0 Ga; Nutman et al., 1992; Jahn et al., 1998), previous WR Sm-Nd isochron ages (2973 ± 48 and 3003 ± 117 Ma; Puchtel and Zhuravlev, 1993), and U–Pb ID-TIMS age of zircons from diorites (3002 ± 5 and 3005 ± 7 Ma; Kovach et al., 2020). The age data are summarized from comparison in Supplementary Table S6.

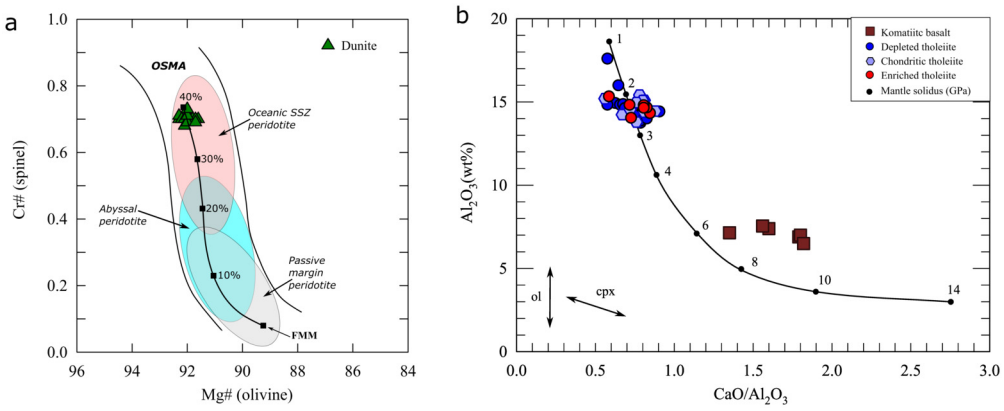

Fig. 7. (a) Cr# in spinel versus Fo content of olivine in fresh dunites from the OGB. Fields for spinels occurring in abyssal peridotites, oceanic SSZ peridotites, and passive-margin peridotites are after Dick and Bullen (1984) and Pearce et al. (2000). The OSMA field is after Arai (1994a; 1994b). (b) Al_2O_3 versus CaO/Al_2O_3 diagram from Herzberg (1995) showing the pressure in GPa (numbers 1 to 14) along the experimentally determined mantle solidus. Komatiitic basalts locate above the solidus at around 6.5∼9 GPa with their elevated Al_2O_3 but constant CaO/Al_2O_3. According to Herzberg (1995), due to most komatiites suffered from olivine cumulates primary komatiite magmas are never preserved (Nisbet et al., 1993). Thus, removal of olivines slightly increases Al_2O_3 contents (Fig. 3b in Herzberg (1995)). The komatiitic basalts in this study have Mg# values (67-71) almost the same with that (∼65-72) of primary magma, which is likely resulted from olivine cumulate to certain extent. Because olivine contains small amounts of CaO and Al_2O_3, their ratio remains intact.

5.2.2. Komatiitic basalts and chondritic tholeiites: mantle plume

The komatiitic basalts in the eastern branch of the OGB were classified as Al-depleted type, which displays depletion in Al and Y relative to Ca and Ti, and in Gd relative to Yb (Puchtel and Zhuravlev, 1993). Komatiitic basalts in this study also show similar characteristics, with high MgO (14–15 wt.%), low Al_2O_3 content (∼7wt.%) and Al_2O_3/TiO_2 ratio (∼10). The depth where magma segregation occurred can be constrained using their Al_2O_3 and CaO/Al_2O_3 correlation (Herzberg, 1995). In the Al_2O_3 vs. CaO/Al_2O_3 diagram (Fig. 7b), komatiitic basalts plot above the solidus line at around 6.5–9 GPa, corresponding to a melt segregation depth at approximately 200–250 km, whereas all tholeiitic basalts cluster close to the solidus line between 2 and 3 GPa (∼60–90 km). The deeper mantle source hinted by above depth of melt segregation of Al-depleted komatiitic basalts, which shows depletion in HREE (Gd/Yb_n = 1.1–1.5; Figs. 5a and 5b) as a result of their mantle source in the garnet stability field, requires a mantle plume to transport and melt at such a depth.

Chondritic tholeiites show flat chondrite-normalized REE patterns with $(La/Yb)_n$, $(La/Sm)_n$, and $(Gd/Yb)_n$ lying between 0.9 and 1.1. Their average immobile element ratios are almost identical to that of the primitive mantle (PM), i.e., Zr/Hf = 34 versus PM = 36, Ti/Zr = 105 versus PM = 115, Sm/Nd = 0.33 versus PM = 0.33, and Lu/Hf = 0.21 versus PM = 0.24. In the Th/Yb vs. Nb/Yb diagram (Fig. 8), both komatiitic basalts and chondritic tholeiites plot close to the PM field, suggesting that their mantle sources might be comparable to that of the proposed primitive mantle but distinct from the modern depleted MORB mantle source. The $\varepsilon Nd_{(t)}$ values of komatiitic basalts range between +1.4 and +2.9, whereas the $\varepsilon Nd_{(t)}$ values of chondritic tholeiites range from +1.5 to higher +3.8. The latter with higher $\varepsilon Nd_{(t)}$ may reflect the interaction between the deeper primitive mantle and the shallower depleted mantle.

5.2.3. Depleted tholeiites: evidence for depleted Archean mantle

Distinct from the modern N-MORB mantle, Archean mafic rocks showing undepleted REE patterns have led to the conclusion that the Archean upper mantle is less depleted than the modern upper mantle (Condie, 1976; Moyen and Laurent, 2018). In contrast, the Olondo depleted tholeiites display a similar REE pattern to modern N-MORB, but with 2 to 4 times lower abundance (Fig. 5e). In the Th/Yb vs. Nb/Yb diagram (Fig. 8), depleted tholeiites plot within or close to the N–MORB field. In addition, these depleted tholeiites are characterized by positive $\varepsilon_{Nd}(t)$ values ranging from +1.8

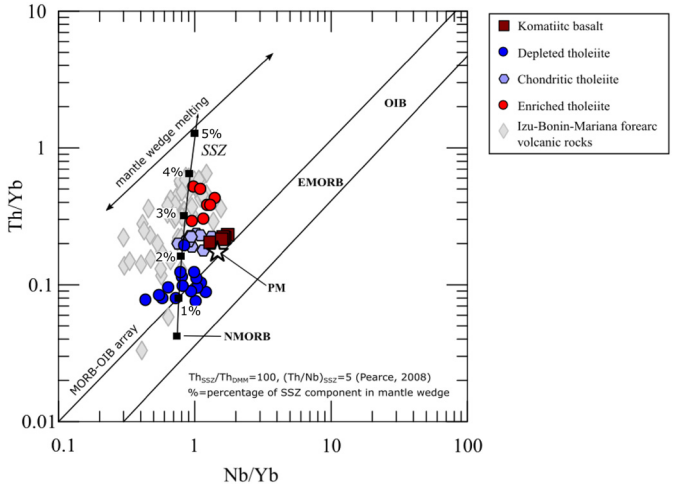

Fig. 8. Th/Yb-Nb/Yb diagram (Pearce, 2008) showing the SSZ enrichment from the MORB-OIB mantle array with percentages of the SSZ component.

to +3.2 and plotting within the depleted mantle array (Goldstein and Jacobsen, 1988; Fig. S2), which could be similar to the modern oceanic crust generated from the upper mantle during the Archean time. All these results suggest that part of the Archean mantle, at least on a local scale, was heterogeneously depleted, even more so than the modern N–MORB mantle, evidenced from the lower REE abundance observed in the Olondo depleted tholeiites. Nevertheless, how the Archean mantle could be more depleted than the modern N–MORB mantle remains unclear. A similar example was also observed in the mafic volcanic rocks from the Ivisaartoq–Ujarassuit greenstone belt, southwestern Greenland (Polat et al., 2011), where the depleted magma was believed to be a result of large-volume melt extraction and re-enrichment by mixing with deeper and less depleted magma. This may be the case for the OGB, where vigorous magmatic activity occurs at 3.0 Ga, and further investigation is needed.

5.2.4. Enriched tholeiites: arc magmatism at subduction initiation stage

Olondo tholeiitic basalts have been studied previously (e.g., Puchtel and Zhuravlev, 1993; Jahn et al., 1998; Puchtel, 2004), however, enriched tholeiites have only been described in Puchtel and Zhuravlev (1993), which was referred to as the Northern Tholeiites. Enriched tholeiites reported in this study display frac-

tionated REE and trace-element patterns as characterized by enrichment of LILE and LREE, and pronounced negative HFSE (Nb, Ta and Ti) anomalies. These features can be attributed to either subduction-related processes or crustal contamination. However, the Olondo tholeiitic basalts might not be affected by crustal contamination as mentioned above. It is believed that the enriched tholeiites were formed in an arc-related environment, where the mantle wedge was metasomatized by slab-derived fluid (dehydration fluid)/melt (recycled crustal sediment). These enriched tholeiites show geochemical characteristics similar to arc tholeiites in the Izu-Bonin-Mariana forearc setting (Figs. 5e and 5f). Both show negative Nb, Ta and Ti, and positive Th, Zr and Hf anomalies in the spidergrams. The distinctive enrichment of Zr is not common in typical arc-related volcanics, but has been recognized in several boninites (Murton et al., 1992). Such an enrichment is similar to IBM boninite, which originated from melt in mantle wedge metasomatized by dehydration fluid and/or melt of recycled continental sediment at the stage of subduction initiation. In the Th/Yb vs. Nb/Yb diagram (Fig. 8), the Olondo enriched tholeiites deviate from the MORB-OIB array with Th enrichment, towards the SSZ field with 3–4% addition of subduction component.

5.2.5. Petrogenetic link between mafic komatiitic-tholeiitic basalts and ultramafic residual dunites

It is challenging to put forward whether OGB komatiitic-tholeiitic basalts and residual dunites have a petrogenetic link because the dunite bodies display a clear tectonic contact with the country rocks in the field as previously mentioned. Geochemically part of residual lithospheric mantle represented by the OGB Nb-depleted dunites were metasomatized by dehydration fluid/melt of recycled continental sediment in a subduction zone, whereas other part as the OGB Nb-undepleted dunites were percolated by basaltic melt from the asthenosphere underneath. The former might be residual mantle after extraction of enriched tholeiites in the mantle wedge, similar to that of modern subduction zones. On the other hand, the latter could be metasomatized lithospheric mantle by filtration of plume-related komatiitic basalts and/or chondritic tholeiites because neither depleted tholeiitic melt could re-enrich its LILE and LREE contents, nor it could be mantle source of komatiitic basalts and chondritic tholeiites.

5.3. Geodynamic implication

The formation of the OGB remains controversial as in the case of other Archean greenstone belts worldwide. Several models have been proposed for the OGB as mentioned above. From the most updated data Puchtel (2004) suggested that OGB could be one of the oldest ophiolitic sequences. Ophiolites are fragments of the upper mantle and oceanic crust (Dewey and Bird, 1971; Coleman, 1977) that were incorporated into continental margins during continent-continent and arc-continent collisions (Dilek and Flower, 2003), ridge-trench interactions (Lagabrielle et al., 2000), and/or subduction-accretion events (Cawood et al., 2009). They are direct witnesses of the forces involved in plate tectonics. Whether the OGB represents ophiolites has become a critical argument if plate tectonics was in operation at $\sim$ 3 Ga when the OGB formed. Considering its abundance (30–40 vol.%) of a great diversity of mafic-ultramafic rocks and volcanic-sedimentary rocks of intermediate and felsic compositions, it is highly possible that the OGB might be the Archean analog as the modern ophiolites, even though it may not be a complete ophiolite suite due to lack of key components such as sheeted dykes, but pillow-like structure might still be preserved (Fig. 2b).

The “arc signature” with Nb depletion in Archean tholeiites has been shown in many studies and could indicate presence of the subduction environment during the Archean time (Polat and Kerrich, 2000; Polat et al., 2002; Dey et al., 2018; Sotiriou et al., 2022). However, it is not always accepted as convincing evidence for subduction because these rocks are sensitive to crustal contamination under a high geothermal condition, thus conclusion that no subduction took place in the Archean had been proposed (e.g., Barley, 1986; Barnes and Arndt, 2019). In contrast, Nb depletion was observed in both OGB dunites and enriched tholeiites in this study. Even though it might not be convincing enough that the OGB enriched tholeiites are free of crustal contamination, nor they formed from melting of fertile or enriched mantle, mafic underplate or lowermost felsic crust. However, it is unlikely for the OGB dunites, representing exposed residual lithospheric mantle, to be affected by crustal contamination and hence best explained to be metasomatized by dehydration fluid/melt of recycled continental sediment in the mantle wedge as in modern subduction zones. As a result, from the mantle perspective the OGB is most likely the Archean analog to modern SSZ ophiolites, which was also proposed by Puchtel (2004). Thus, it is evident that the subduction was in operation in the Mesoarchean time.

The overall geochemical characteristics of the OGB ultramafic-mafic rocks indicate their petrogenesis requires tectonic settings similar to modern subduction zone, more specifically at subduction initiation stage for dunites and enriched tholeiites; mid-ocean ridge for depleted tholeiites; and mantle plume for komatiitic basalts and chondritic tholeiites. A novel hypothesis that the impingement of a mantle plume head on the base of the lithosphere can cause a new subduction zone to form is recently proposed plume-induced subduction initiation (PISI; Whattam and Stern, 2015 and references therein). Gerya et al. (2015) further proposed that formation of a new subduction zone as a result of plume-lithosphere interaction can address the earliest subduction and the beginning of plate tectonics on Earth. The OGB ultramafic-mafic rocks could be a record to witness such plume-induced subduction initiation processes in the Mesoarchean time. Proposed tectonic settings for the OGB ultramafic-mafic rocks to fit the PISI scenario are illustrated in the schematic model (Fig. 9). Numerical modeling shows that for newly-formed continental lithosphere on the early Earth, plume material penetrated through this overlying lithosphere causing rupture in the crust. Subsequent subduction initiation and lithosphere sinking all take only a few million years (Cloetingh et al., 2021). Such short time span indicates different types of magmas associated with mantle plume, crustal rupture (mid-ocean ridge) and subduction initiation could be generated within few million years. This could explain whole-rock Sm-Nd isochron ages (2973 ± 48 and 3003 ± 117 Ma; Puchtel and Zhuravlev, 1993) of the OGB mafic rocks are similar to Os T_{MA} model age of 2959 to 3020 Ma of the OGB dunites, both are around 3 Ga. At that time a proposed mantle plume that ruptured the Olekma TTG complex in the continental crust to generate the OGB komatiitic basalt via melting at a deeper depth and chondritic tholeiites via melting at a shallower depth (①② in Fig. 9). These two magmas also metasomatized residual lithospheric mantle to form the OGB Nb-undepleted dunites on the way to surface (③ in Fig. 9). The rupture of continental crust induced mid-ocean ridge-like setting to generate oceanic crust represented by the OGB depleted tholeiites (④ in Fig. 9), and the residual lithospheric mantle mentioned above. Subsequent subduction initiation provided dehydration fluid and/or melt of recycled continental sediment to metasomatize mantle wedge to generate boninite-like OGB enriched tholeiites (⑤ in Fig. 9), and its residual lithospheric mantle representing by the OGB Nb-depleted dunites (⑥ in Fig. 9).

6. Conclusions

(1) The OGB Nb-depleted dunites, representing exposed ancient residual lithospheric mantle, were metasomatized by dehydration

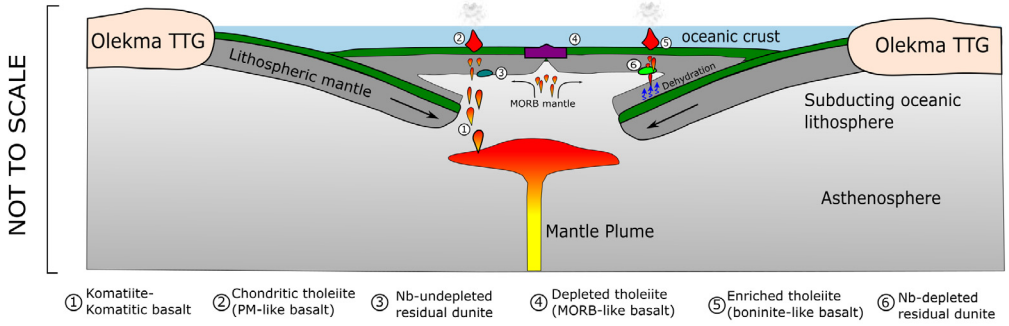

Fig. 9. Schematic model showing genesis of residue dunites and komatiitic-tholeiitic basalts in a plume-induced subduction initiation (PISI) setting. A proposed mantle plume penetrated the existing Olekma continental block to rupture it then generate oceanic crust and initiate subduction subsequently.

fluid/melt of recycled continental sediment in the mantle wedge as in modern subduction zones.

(2) The Os model ages of the residue dunites are estimated to be around 3 Ga, the same age as the OGB formation, which is determined by U-Pb dating of zircons from the felsic meta-volcanic rocks.

(3) The overall geochemical characteristics of the OGB ultramafic-mafic rocks indicate their petrogenesis requires tectonic settings such as the subduction zone, more specifically at subduction initiation stage for dunites and enriched tholeiites; mid-ocean ridge for depleted tholeiites; and mantle plume for komatiitic basalts and chondritic tholeiites.

(4) The OGB ultramafic-mafic rocks could be a record to witness plume-induced subduction initiation processes such as mantle plume, sea-floor spreading and subduction were in operation in the Mesoarchean time.

CRediT authorship contribution statement

Thi-Duyen Tran: Data curation, Formal analysis, Investigation, Visualization, Writing – original draft. **Kuo-Lung Wang:** Conceptualization, Funding acquisition, Supervision, Writing – review & editing. **Victor Kovach:** Conceptualization, Funding acquisition, Supervision. **Alexander Kotov:** Conceptualization, Project administration, Supervision. **Sergey Velikoslavinsky:** Investigation, Validation. **Nikolay Popov:** Investigation, Validation. **Sergey Dril:** Investigation, Validation. **Zhu-Yin Chu:** Methodology. **Der-Chuen Lee:** Conceptualization, Writing – review & editing. **Li-Wei Kuo:** Project administration, Supervision. **Yoshiyuki Iizuka:** Data curation, Methodology, Resources. **Hao-Yang Lee:** Data curation, Methodology, Resources.

Declaration of competing interest

The authors declare that they have no known competing financial interests or personal relationships that could have appeared to influence the work reported in this paper.

Data availability

Data will be made available on request.

Acknowledgements

We thank C-Y. Lee at the Department of Geosciences, National Taiwan University, Taipei; Fu-Lung Lin, Yu-Shiang Wang, and Emily Hung at IES, Academia Sinica, Taipei and N. Zagornaya at IPGG RAS, St. Petersburg, Russia for their analytical assistance. T-D. T. is grateful for receiving funds from the Taiwan International Graduate Program (TIGP)–Earth System Science Program, Academia Sinica and National Central University, Taiwan. Constructive review comments from Editor Rosemary Hickey-Vargas, Igor Puchtel and two anonymous reviewers have improved the presentation of various aspects of this manuscript. This study was supported by research grants from Academia Sinica, Taiwan (AS-CDA-107-M01), the Ministry of Science and Technology, Taiwan (NSC102-2628-M-001-006-MY4), the Russian Foundation for Basic Research (18-55-52001), and IPGG Russian Academy of Sciences (FMUW-2022-0003). This is No. IESAS 2412 publication of Institute of Earth Sciences, Academia Sinica.

Appendix. Supplementary material

Supplementary material related to this article can be found online at https://doi.org/10.1016/j.epsl.2022.117975.

References

Arai, S., 1994a. Characterization of spinel peridotites by olivine-spinel compositional relationships: review and interpretation. Chem. Geol. 113, 191–204.
Arai, S., 1994b. Compositional variation of olivine-chromian spinel in Mg-rich magmas as a guide to their residual spinel peridotites. J. Volcanol. Geotherm. Res. 59, 279–293.
Arndt, N.T., Lesher, C.M., Barnes, S.J., 2008. Komatiite. Cambridge University Press, Cambridge.
Aswad, K.J., Aziz, N.R., Koyi, H.A., 2011. Cr-spinel compositions in serpentinites and their implications for the petrotectonic history of the Zagros Suture Zone, Kurdistan Region, Iraq. Geol. Mag. 148, 802–818.
Ballhaus, C., Berry, R.F., Green, D.H., 1991. High pressure experimental calibration of the olivine-orthopyroxene-spinel oxygen geobarometer: implications for the oxidation state of the upper mantle. Contrib. Mineral. Petrol. 107 (1), 27–40.
Barley, M.E., 1986. Incompatible-element enrichment in Archean basalts: a consequence of contamination by older sialic crust rather than mantle heterogeneity. Geology 14 (11), 947–950.
Barnes, S.J., Arndt, N.T., 2019. Distribution and geochemistry of komatiites and basalts through the Archean. In: Van Kranendonk, M.J., Bennett, V.C., Hoffmann, E. (Eds.), Earth's Oldest Rocks, 2nd ed. Elsevier, pp. 103–132.
Bibikova, E.V., Kirnozova, T.I., Makarov, V.A., Drugova, G.M., Bushmin, S.A., 1984. The time of volcanism in the Olondo greenstone-belt (East-Siberia). Dokl. Akad. Nauk SSSR 279 (6), 1424–1428.
Bogomolova, L.M., 1993. Extended Abstract of Candidate's Dissertation in Geology and Mineralogy. Trofimuk Inst. Petrol. Geol. Geophys., Siberian Branch RAS, Novosibirsk (in Russian).
Braun, J.-J., Pagel, M., Herbilln, A., Rosin, C., 1993. Mobilization and redistribution of REEs and thorium in a syenitic lateritic profile: a mass balance study. Geochim. Cosmochim. Acta 57, 4419–4434.
Cawood, P.A., Kröner, A., Collins, W.J., Kusky, T.M., Mooney, W.D., Windley, B.F., 2009. Accretionary orogens through Earth history. Geol. Soc. (Lond.) Spec. Publ. 318 (1), 1–36.
Cloetingh, S., Koptev, A., Kovács, I., Gerya, T., Beniest, A., Willingshofer, E., Ehlers, T.A., Andrić-Tomašević, N., Botsyun, S., Eizenhöfer, P.R., François, T., 2021. Plume-induced sinking of intracontinental lithospheric mantle: an overlooked mechanism of subduction initiation? Geochem. Geophys. Geosyst. 22 (2), e2020GC009482.
Coleman, R.G., 1977. What is an ophiolite? In: Ophiolites. Springer, Berlin, Heidelberg, pp. 1–7.
Condie, K.C., 1976. Trace-element geochemistry of Archean greenstone belts. Earth-Sci. Rev. 12, 393–417.
de Wit, M.J., 2004. Archean greenstone belts do contain fragments of ophiolites. Dev. Precambrian Geol. 13, 599–614.

Dewey, J.F., Bird, J.M., 1971. Origin and emplacement of the ophiolite suite: Appalachian ophiolites in Newfoundland. J. Geophys. Res. 76 (14), 3179–3206.
Dey, S., Pal, S., Balakrishnan, S., Halla, J., Kurhila, M., Heilimo, E., 2018. Both plume and arc: origin of Neoarchaean crust as recorded in Veligallu greenstone belt, Dharwar craton, India. Precambrian Res. 314, 41–61.
Dick, H.J., Bullen, T., 1984. Chromian spinel as a petrogenetic indicator in abyssal and alpine-type peridotites and spatially associated lavas. Contrib. Mineral. Petrol. 86, 54–76.
Dilek, Y., Flower, M.F., 2003. Arc-trench rollback and forearc accretion: 2. A model template for ophiolites in Albania, Cyprus, and Oman. Geol. Soc. (Lond.) Spec. Publ. 218 (1), 43–68.
Furnes, H., de Wit, M., Dilek, Y., 2014. Precambrian greenstone belts host different ophiolite types. In: Evolution of Archean Crust and Early Life. Springer, pp. 1–22.
Garde, A.A., Windley, B.F., Kokfelt, T.F., Keulen, N., 2020. Archaean plate tectonics in the North Atlantic craton of West Greenland revealed by well-exposed horizontal crustal tectonics, island arcs and tonalite-trondhjemite-granodiorite complexes. Front. Earth Sci. 8, 540997.
Gerya, T.V., Stern, R.J., Baes, M., Sobolev, S.V., Whattam, S.A., 2015. Plate tectonics on the Earth triggered by plume-induced subduction initiation. Nature 527 (7577), 221–225.
Goldstein, S.J., Jacobsen, S.B., 1988. Nd and Sr isotopic systematics of rivers water suspended material: implications for crustal evolution. Earth Planet. Sci. Lett. 87, 249–265.
Grachev, A., Fedorovsky, V., 1981. On the nature of greenstone belts in the Precambrian. In: Developments in Geotectonics. Elsevier, pp. 195–212.
Green, D., Ringwood, A., 1967. The genesis of basaltic magmas. Contrib. Mineral. Petrol. 15, 103–190.
Grocolas, T., Bouilhol, P., Caro, G., Mojzsis, S.J., 2022. Eoarchean subduction-like magmatism recorded in 3750 Ma mafic–ultramafic rocks of the Ukaliq supracrustal belt (Québec). Contrib. Mineral. Petrol. 177 (3), 1–27.
Grosch, E.G., Slama, J., 2017. Evidence for 3.3-billion-year-old oceanic crust in the Barberton greenstone belt, South Africa. Geology 45 (8), 695–698.
Hanmer, S., Greene, D.C., 2002. A modern structural regime in the Paleoarchean (∼ 3.64 Ga); Isua greenstone belt, southern West Greenland. Tectonophysics 346 (3–4), 201–222.
Herzberg, C., 1995. Generation of plume magmas through time: an experimental perspective. Chem. Geol. 126 (1), 1–16.
Hyung, E., Jacobsen, S.B., 2020. The 142Nd/144Nd variations in mantle-derived rocks provide constraints on the stirring rate of the mantle from the Hadean to the present. Proc. Natl. Acad. Sci. 117 (26), 14738–14744.
Jahn, B.-M., Gruau, G., Capdevila, R., Cornichet, J., Nemchin, A., Pidgeon, R., Rudnik, V., 1998. Archean crustal evolution of the Aldan Shield, Siberia: geochemical and isotopic constraints. Precambrian Res. 91, 333–363.
Jensen, L.S., Pyke, D.R., 1982. Komatiites in the Ontario portion of the Abitibi belt. In: Arndt, N.T., Nisbet, E.G. (Eds.), Komatiites. George Allen & Unwin, London, pp. 147–157.
Komiya, T., Yamamoto, S., Aoki, S., Sawaki, Y., Ishikawa, A., Tashiro, T., Koshida, K., Shimojo, M., Aoki, K., Collerson, K.D., 2015. Geology of the Eoarchean, > 3.95 Ga, Nulliak supracrustal rocks in the Saglek Block, northern Labrador, Canada: the oldest geological evidence for plate tectonics. Tectonophysics 662, 40–66.
Kotov, A.B., 2003. The boundary conditions of geodynamic models for the formation of the continental crust of the Aldan Shield. ScD thesis, 79 p. Extended Abstract of Doctoral Dissertation in Geology and Mineralogy. St. Petersburg State Univ., St. Petersburg.
Kovach, V.P., Kotov, A.B., Salnikova, E.B., Popov, N.V., Velikoslavinsky, S.D., Plotkina, J.V., Wang, K.-L., Fedoseenko, A.M., 2020. The upper age boundary of the formation of the Olondo fragment of the Tokko–Khani greenstone belt, Aldan Shield: U–Pb (ID-TIMS) geochronological data. Dokl. Earth Sci. 494, 767–772.
Kusky, T.M., Li, J.-H., Tucker, R.D., 2001. The Archean Dongwanzi ophiolite complex, North China Craton: 2.505-billion-year-old oceanic crust and mantle. Science 292, 1142–1145.
Kusky, T., Windley, B.F., Polat, A., Wang, L., Ning, W., Zhong, Y., 2021. Archean dome-and-basin style structures form during growth and death of intraoceanic and continental margin arcs in accretionary orogens. Earth-Sci. Rev. 220, 103725.
Lagabrielle, Y., Guivel, C., Maury, R.C., Bourgois, J., Fourcade, S., Martin, H., 2000. Magmatic–tectonic effects of high thermal regime at the site of active ridge subduction: the Chile Triple Junction model. Tectonophysics 326 (3–4), 255–268.
Lahaye, Y., Arndt, N., 1996. Alteration of a komatiite flow from Alexo, Ontario, Canada. J. Petrol. 37, 1261–1284.
McIntyre, T., Pearson, D., Szilas, K., Morishita, T., 2019. Implications for the origins of Eoarchean ultramafic rocks of the North Atlantic Craton: a study of the Tussaap Ultramafic complex, Itsaq Gneiss complex, southern West Greenland. Contrib. Mineral. Petrol. 174, 96.
Moyen, J.-F., Laurent, O., 2018. Archaean tectonic systems: a view from igneous rocks. Lithos 302, 99–125.
Murton, B.J., Peate, D.W., Arculus, R.J., Pearce, J.A., Van der Laan, S., 1992. 12. Trace-element geochemistry of volcanic rocks from Site 786: the Izu-Bonin forearc. In: Proceedings of the Ocean Drilling Program, Scientific Results, vol. 125, pp. 211–235.
Næraa, T., Scherstén, A., Rosing, M.T., Kemp, A., Hoffmann, J., Kokfelt, T., Whitehouse, M., 2012. Hafnium isotope evidence for a transition in the dynamics of continental growth 3.2 Gyr ago. Nature 485, 627–630.
Neymark, L.A., Kovach, V.P., Nemchin, A.A., Morozova, I.M., Kotov, A.B., Vinogradov, D.P., Gorokhovsky, B.M., Ovchinnikova, G.V., Bogomolova, L.M., Smelov, A.P., 1993. Late Archaean intrusive complexes in Olekma granite-greenstone terrain (Eastern Siberia): geochemical and isotopic study. Precambrian Res. 62, 453–472.
Nisbet, E.G., Cheadle, M.J., Arndt, N.T., Bickle, M.J., 1993. Constraining the potential temperature of the Archaean mantle: a review of the evidence from komatiites. Lithos 30, 291–307.
Nutman, A.P., Friend, C.R., 2009. New 1:20,000 scale geological maps, synthesis and history of investigation of the Isua supracrustal belt and adjacent orthogneisses, southern West Greenland: a glimpse of Eoarchaean crust formation and orogeny. Precambrian Res. 172 (3–4), 189–211.
Nutman, A.P., Chenyshev, I.V., Baadsgaard, H., Smelov, A.P., 1992. The Aldan Shield of Siberia, USSR: the age of its Archaean components and evidence for widespread reworking in the mid-Proterozoic. Precambrian Res. 54, 195–210.
Nutman, A.P., Bennett, V.C., Friend, C.R., Yi, K., 2020. Eoarchean contrasting ultra-high-pressure to low-pressure metamorphisms (< 250 to > 1000 °C/GPa) explained by tectonic plate convergence in deep time. Precambrian Res. 344, 105770.
Nutman, A.P., Bennett, V.C., Friend, C.R., Polat, A., Hoffmann, E., Van Kranendonk, M., 2021a. Fifty years of the Eoarchean and the case for evolving uniformitarianism. Precambrian Res. 367, 106442.
Nutman, A.P., Scicchitano, M.R., Friend, C.R., Bennett, V.C., Chivas, A.R., 2021b. Isua (Greenland) ∼ 3700 Ma meta-serpentinite olivine Mg# and δ18O signatures show connection between the early mantle and hydrosphere: geodynamic implications. Precambrian Res. 361, 106249.
Parkinson, I.J., Pearce, J.A., 1998. Peridotites from the Izu–Bonin–Mariana forearc (ODP Leg 125): evidence for mantle melting and melt–mantle interaction in a supra-subduction zone setting. J. Petrol. 39 (9), 1577–1618.
Pearce, J.A., 2008. Geochemical fingerprinting of oceanic basalts with applications to ophiolite classification and the search for Archean oceanic crust. Lithos 100, 14–48.
Pearce, J.A., Barker, P., Edwards, S., Parkinson, I., Leat, P., 2000. Geochemistry and tectonic significance of peridotites from the South Sandwich arc–basin system, South Atlantic. Contrib. Mineral. Petrol. 139, 36–53.
Polat, A., Hofmann, A., 2003. Alteration and geochemical patterns in the 3.7–3.8 Ga Isua greenstone belt, West Greenland. Precambrian Res. 126, 197–218.
Polat, A., Kerrich, R., 2000. Archean greenstone belt magmatism and the continental growth–mantle evolution connection: constraints from Th–U–Nb–LREE systematics of the 2.7 Ga Wawa subprovince, Superior Province, Canada. Earth Planet. Sci. Lett. 175 (1–2), 41–54.
Polat, A., Hofmann, A., Rosing, M.T., 2002. Boninite-like volcanic rocks in the 3.7–3.8 Ga Isua greenstone belt, West Greenland: geochemical evidence for intra-oceanic subduction zone processes in the early Earth. Chem. Geol. 184, 231–254.
Polat, A., Appel, P.W., Fryer, B.J., 2011. An overview of the geochemistry of Eoarchean to Mesoarchean ultramafic to mafic volcanic rocks, SW Greenland: implications for mantle depletion and petrogenetic processes at subduction zones in the early Earth. Gondwana Res. 20, 255–283.
Popov, N.V., Smelov, A.P., Dobretsov, N.N., Bogomolova, L.M., Kartavchenko, V.G., 1990. The Olondo Greenstone Belt. Izd. Yakutskogo Nauchnogo Tsentra SO AN SSSR, Yakutsk (in Russian).
Popov, N., Dobretsov, N., Smelov, A., Bogomolova, L., 1995. Tectonics, metamorphism, and the problems of evolution of the Olondo greenstone belt. Petrology 3, 73–86.
Puchtel, I.S., 2004. 3.0 Ga Olondo greenstone belt in the Aldan shield, E. Siberia. Dev. Precambrian Geol. 13, 405–423.
Puchtel, I., Zhuravlev, D., 1993. Petrology of mafic-ultramafic metavolcanics and related rocks from the Olondo greenstone belt, Aldan Shield. Petrology 1, 263–299.
Puchtel, I.S., Samsonov, A.V., Simon, A.R., Zhuravlev, D.Z., 1989. Petrology, geochemistry and Sm-Nd age of metavolcanics from the Olondo greenstone belt. In: Dook, V.L., Neymark, L.A., Rudnik, V.A. (Eds.), Excursion Guide for the IGCP Project 280 Titled "The Oldest Rocks of the Aldan-Stanovik Shield, Eastern Siberia, USSR". Leningrad-Mainz, pp. 27–35.
Puchtel, I.S., Frikh-Khar, D.I., Ashikhmina, N.A., Tomashpolskiy, Yw.Ya., Shirina, N.G., 1991. Metamorphic olivines in ultrabasites of Olondin greenstone belt and the problem of identification of komatiites (Aldan Shield). Int. Geol. Rev. 33, 161–173.
Puchtel, I.S., Bogatikov, O.A., Simon, A.K., 1993. The Early Precambrian crust-mantle evolution of the Olekma gneiss-greenstone terrane, Aldan Shield. Petrology 1, 451–473.
Rosen, O.M., Turkina, O.M., 2007. The oldest rock assemblages of the Siberian Craton. Dev. Precambrian Geol. 15, 793–838.
Rundqvist, D.V., Mitrofanov, F.P. (Eds.), 1993. Precambrian Geology of the USSR. Elsevier.
Salnikova, E.B., Kovach, V.P., Kotov, A.B., Nemchin, A.A., 1996. Evolution of continental crust in the Western Aldan Shield: evidence from Sm–Nd systematics of granitoids. Petrology 4, 105–118.

Smelov, A., Shatsky, V., Ragozin, A., Reutskii, V., Molotkov, A., 2012. Diamondiferous Archean rocks of the Olondo greenstone belt (western Aldan–Stanovoy shield). Russ. Geol. Geophys. 53, 1012–1022.
Smith, A., Ludden, J., 1989. Nd isotopic evolution of the Precambrian mantle. Earth Planet. Sci. Lett. 93, 14–22.
Sotiriou, P., Polat, A., Windley, B.F., Kusky, T., 2022. Temporal variations in the incompatible trace element systematics of Archean volcanic rocks: implications for tectonic processes in the early Earth. Precambrian Res. 368, 106487.
Stern, R.J., 2005. Evidence from ophiolites, blueschists, and ultrahigh-pressure metamorphic terranes that the modern episode of subduction tectonics began in Neoproterozoic time. Geology 33 (7), 557–560.
Sun, S.-S., McDonough, W.F., 1989. Chemical and isotopic systematics of oceanic basalts: implications for mantle composition and processes. Geol. Soc. (Lond.) Spec. Publ. 42, 313–345.
Sun, S.-S., Nesbitt, R.W., 1978. Geochemical regularities and genetic significance of ophiolitic basalts. Geology 6, 689–693.
Szilas, K., van Hinsberg, V., McDonald, I., Næraa, T., Rollinson, H., Adetunji, J., Bird, D., 2018. Highly refractory Archaean peridotite cumulates: petrology and geochemistry of the Seqi Ultramafic Complex, SW Greenland. Geosci. Front. 9, 689–714.
Velikoslavinskii, S.D., Kotov, A.B., Salnikova, E.B., Kuznetsov, A.B., Kovach, V.P., Popov, N.V., Tolmacheva, E.V., Anisimova, I.V., Plotkina, Yu.V., 2018. New data on the age of the tonalite–trondhjemite orthogneisses of the Olekma Complex of the central part of the Chara–Olekma geoblock, Aldan Shield. Dokl. Earth Sci. 482, 1265–1269.
Whattam, S.A., Stern, R.J., 2015. Late Cretaceous plume-induced subduction initiation along the southern margin of the Caribbean and NW South America: the first documented example with implications for the onset of plate tectonics. Gondwana Res. 27 (1), 38–63.
Winchester, J., Floyd, P., 1976. Geochemical magma type discrimination: application to altered and metamorphosed basic igneous rocks. Earth Planet. Sci. Lett. 28, 459–469.
Windley, B.F., Kusky, T., Polat, A., 2021. Onset of plate tectonics by the Eoarchean. Precambrian Res. 352, 105980.